



Comparative analysis of transparent conductive oxide electro-absorption modulators [Invited]

QIAN GAO, ERWEN LI, AND ALAN X. WANG*

School of Electrical Engineering and Computer Science, Oregon State University, Corvallis, OR 97331, USA

*wang@oregonstate.edu

Abstract: Electron accumulation in transparent conductive oxides (TCOs), when driven by a gate voltage, is capable of inducing extremely strong electro-optic absorption at the telecommunication wavelength window due to the epsilon-near-zero (ENZ) effect and various waveguide modulators have been proposed in recent years. This paper conducts a comparative analysis of TCO modulators by reviewing several representative designs based on the uniform concentration accumulated carrier model and the classical continuous carrier distribution model. We also apply the quantum moment model to analyze the free carrier distribution of the TCO based metal-oxide-semiconductor (MOS) capacitor for the first time, and reveal significantly different device physics compared with previous simulation models. The quantum moment model predicts a much higher driving voltage in order to turn the TCO materials into ENZ and a stronger modulation strength compared with the classical model. Especially, the requirement of the higher gate voltage brings a great challenge to the insulator layer as the electric field in the insulator is exceeding the breakdown strength, which raises the concern of reliability. In order to evaluate the accuracy of different models, we compare the simulation results with two of the most recent experimental papers and show that the quantum model has a better match in terms of the electro-absorption rate and the differential driving voltage. However, the quantum moment model still cannot explain some other experimental results, which may be induced by different modulation mechanisms.

© 2018 Optical Society of America under the terms of the [OSA Open Access Publishing Agreement](#)

OCIS codes: (250.7360) Waveguide modulators; (130.3130) Integrated optics materials; (160.2100) Electro-optical materials

References and links

1. G. V. Naik, J. Kim, and A. Boltasseva, "Oxides and nitrides as alternative plasmonic materials in the optical range," *Opt. Mater. Express* **1**(6), 1090–1099 (2011).
2. G. V. Naik, V. M. Shalaev, and A. Boltasseva, "Alternative plasmonic materials: beyond gold and silver," *Adv. Mater.* **25**(24), 3264–3294 (2013).
3. J. F. Wager, "Applied physics. Transparent electronics," *Science* **300**(5623), 1245–1246 (2003).
4. T. Minami, "Transparent conducting oxide semiconductors for transparent electrodes," *Semicond. Sci. Technol.* **20**(4), S35–S44 (2005).
5. E. Feigenbaum, K. Diest, and H. A. Atwater, "Unity-order index change in transparent conducting oxides at visible frequencies," *Nano Lett.* **10**(6), 2111–2116 (2010).
6. I. Liberal and N. Engheta, "Near-zero refractive index photonics," *Nat. Photonics* **11**(3), 149–158 (2017).
7. M. Z. Alam, I. De Leon, and R. W. Boyd, "Large optical nonlinearity of indium tin oxide in its epsilon-near-zero region," *Science* **352**(6287), 795–797 (2016).
8. J. Park, J. H. Kang, X. Liu, and M. L. Brongersma, "Electrically tunable epsilon-near-zero (ENZ) metafilm absorbers," *Sci. Rep.* **5**(1), 15754 (2015).
9. N. Kinsey, C. DeVault, J. Kim, M. Ferrera, V. M. Shalaev, and A. Boltasseva, "Epsilon-near-zero Al-doped ZnO for ultrafast switching at telecom wavelengths," *Optica* **2**(7), 616–622 (2015).
10. J. Park, J. H. Kang, X. Liu, and M. L. Brongersma, "Electrically tunable epsilon-near-zero (ENZ) metafilm absorbers," *Sci. Rep.* **5**(1), 15754 (2015).
11. Y. Yang, K. Kelley, E. Sachet, S. Campione, T. S. Luk, J. P. Maria, M. B. Sinclair, and I. Brener, "Femtosecond optical polarization switching using a cadmium oxide-based perfect absorber," *Nat. Photonics* **11**(6), 390–395 (2017).
12. Y. Yao, R. Shankar, M. A. Kats, Y. Song, J. Kong, M. Loncar, and F. Capasso, "Electrically tunable metasurface

- perfect absorbers for ultrathin mid-infrared optical modulators,” *Nano Lett.* **14**(11), 6526–6532 (2014).
13. E. Li, Q. Gao, R. T. Chen, and A. X. Wang, “Ultra-compact silicon-conductive oxide nano-cavity modulator with 0.02 lambda-cubic active volume,” *Nano Lett.* **18**(2), 1075–1081 (2018).
 14. S. Campione, M. G. Wood, D. K. Serkland, S. Parameswaran, J. Ihlefeld, T. S. Luk, J. R. Wendt, K. M. Geib, and G. A. Keeler, “Submicrometer epsilon-near-zero electroabsorption modulators enabled by high-mobility cadmium oxide,” *IEEE Photonics J.* **9**(4), 1–7 (2017).
 15. A. P. Vasudev, J. H. Kang, J. Park, X. Liu, and M. L. Brongersma, “Electro-optical modulation of a silicon waveguide with an “epsilon-near-zero” material,” *Opt. Express* **21**(22), 26387–26397 (2013).
 16. J. Baek, J. B. You, and K. Yu, “Free-carrier electro-refraction modulation based on a silicon slot waveguide with ITO,” *Opt. Express* **23**(12), 15863–15876 (2015).
 17. S. Zhu, G. Q. Lo, and D. L. Kwong, “Design of an ultra-compact electro-absorption modulator comprised of a deposited TiN/HfO₂/ITO/Cu stack for CMOS backend integration,” *Opt. Express* **22**(15), 17930–17947 (2014).
 18. M. Ayata, Y. Nakano, and T. Tanemura, “Silicon rib waveguide electro-absorption optical modulator using transparent conductive oxide bilayer,” *Jpn. J. Appl. Phys.* **55**(4), 042201 (2016).
 19. H. Zhao, Y. Wang, A. Capretti, L. Dal Negro, and J. Klamkin, “Broadband electroabsorption modulators design based on epsilon-near-zero indium tin oxide,” *IEEE J. Sel. Top. Quantum Electron.* **21**(4), 192–198 (2015).
 20. Z. Lu, W. Zhao, and K. Shi, “Ultrapact electroabsorption modulators based on tunable epsilon-near-zero-slot waveguides,” *IEEE Photonics J.* **4**(3), 735–740 (2012).
 21. V. E. Babicheva, N. Kinsey, G. V. Naik, M. Ferrera, A. V. Lavrinenko, V. M. Shalaev, and A. Boltasseva, “Towards CMOS-compatible nanophotonics: Ultra-compact modulators using alternative plasmonic materials,” *Opt. Express* **21**(22), 27326–27337 (2013).
 22. A. O. Zaki, K. Kirah, and M. A. Swillam, “Hybrid plasmonic electro-optical modulator,” *Appl. Phys., A Mater. Sci. Process.* **122**(4), 473 (2016).
 23. C. Huang, R. J. Lamond, S. K. Pickus, Z. R. Li, and V. J. Sorger, “A sub- λ -size modulator beyond the efficiency-loss limit,” *IEEE Photonics J.* **5**(4), 2202411 (2013).
 24. U. Koch, C. Hössbacher, J. Niegemann, C. Hafner, and J. Leuthold, “Digital plasmonic absorption modulator exploiting epsilon-near-zero in transparent conducting oxides,” *IEEE Photonics J.* **8**(1), 1–13 (2016).
 25. A. V. Krasavin and A. V. Zayats, “Photonic signal processing on electronic scales: electro-optical field-effect nanoplasmonic modulator,” *Phys. Rev. Lett.* **109**(5), 053901 (2012).
 26. G. Sinatkas, A. Pitolakis, D. C. Zografopoulos, R. Beccherelli, and E. E. Kriezis, “Transparent conducting oxide electro-optic modulators on silicon platforms: A comprehensive study based on the drift-diffusion semiconductor model,” *J. Appl. Phys.* **121**(2), 023109 (2017).
 27. H. W. Lee, G. Papadakis, S. P. Burgos, K. Chander, A. Kriesch, R. Pala, U. Peschel, and H. A. Atwater, “Nanoscale conducting oxide PlasMOStor,” *Nano Lett.* **14**(11), 6463–6468 (2014).
 28. V. J. Sorger, N. D. Lanzillotti-Kimura, R. M. Ma, and X. Zhang, “Ultra-compact silicon nanophotonic modulator with broadband response,” *Nanophotonics* **1**(1), 17–22 (2012).
 29. M. G. Wood, S. Campione, S. Parameswaran, T. S. Luk, J. R. Wendt, D. K. Serkland, and G. A. Keeler, “Gigahertz speed operation of epsilon-near-zero silicon photonic modulators,” *Optica* **5**(3), 233–236 (2018).
 30. Z. Lu, K. Shi, and P. Yin, “Nanoscale field effect optical modulators based on depletion of epsilon-near-zero films,” *Opt. Commun.* **381**, 18–23 (2016).
 31. Q. Gao, E. Li, and A. X. Wang, “Ultra-compact and broadband electro-absorption modulator using an epsilon-near-zero conductive oxide,” *Photon. Res.* **6**(4), 277–281 (2018).
 32. R. Resta, “Thomas-Fermi dielectric screening in semiconductors,” *Phys. Rev. B* **16**(6), 2717–2722 (1977).
 33. J. A. Schuller, E. S. Barnard, W. Cai, Y. C. Jun, J. S. White, and M. L. Brongersma, “Plasmonics for extreme light concentration and manipulation,” *Nat. Mater.* **9**(3), 193–204 (2010).
 34. J. Yota, H. Shen, and R. Ramanathan, “Characterization of atomic layer deposition HfO₂, Al₂O₃, and plasma-enhanced chemical vapor deposition Si₃N₄ as metal–insulator–metal capacitor dielectric for GaAs HBT technology,” *J. Vac. Sci. Technol. A* **31**(1), 01A134 (2013).
 35. A. Wettstein, A. Schenk, and W. Fichtner, “Quantum device-simulation with the density-gradient model on unstructured grids,” *IEEE Trans. Electron Dev.* **48**(2), 279–284 (2001).
 36. W. Hänsch, T. Vogelsang, R. Kircher, and M. Orlowski, “Carrier transport near the Si/SiO₂ interface of a MOSFET,” *Solid-State Electron.* **32**(10), 839–849 (1989).
 37. Silvaco Inc, ATLAS user’s manual—Device simulator software (Silvaco Inc. 2013).
 38. H. Kim, C. M. Gilmore, A. Pique, J. S. Horwitz, H. Mattoussi, H. Murata, Z. H. Kafafi, and D. B. Chrisey, “Electrical, optical, and structural properties of indium–tin–oxide thin films for organic light-emitting devices,” *J. Appl. Phys.* **86**(11), 6451–6461 (1999).
 39. G. G. Pethuraja, R. E. Welsler, A. K. Sood, C. Lee, N. J. Alexander, H. Efstathiadis, P. Haldar, and J. L. Harvey, “Current-voltage characteristics of ITO/p-Si and ITO/n-Si contact interfaces,” *Adv. Mater. Phys. Chem.* **2**(2), 59 (2012).
 40. I. Hamberg and C. G. Granqvist, “Evaporated Sn-doped In₂O₃ films: Basic optical properties and applications to energy-efficient windows,” *J. Appl. Phys.* **60**(11), R123–R160 (1986).
 41. J. R. Zhou and D. K. Ferry, “Simulation of Ultra-small GaAs MESFET Using Quantum Moment Equations,” *IEEE Trans. Electron Dev.* **39**(3), 473–478 (1992).
 42. A. Wettstein, A. Schenk, and W. Fichtner, “Quantum device-simulation with the density gradient model on unstructured grids,” *IEEE Trans. Electron Dev.* **48**(2), 279–284 (2001).

43. C. Hoessbacher, Y. Fedoryshyn, A. Emboras, A. Melikyan, M. Kohl, D. Hillerkuss, C. Hafner, and J. Leuthold, "The plasmonic memristor: a latching optical switch," *Optica* **1**(4), 198–202 (2014).
44. K. Thyagarajan, R. Sokhoyan, L. Zornberg, and H. A. Atwater, "Millivolt modulation of plasmonic metasurface optical response via ionic conductance," *Adv. Mater.* **29**(31), 1701044 (2017).
45. B. N. Behnken, G. Karunasiri, D. R. Chamberlin, P. R. Robrish, and J. Faist, "Real-time imaging using a 2.8 THz quantum cascade laser and uncooled infrared microbolometer camera," *Opt. Lett.* **33**(5), 440–442 (2008).
46. D. Bohm, "A suggested interpretation of the quantum theory in terms of "hidden" variables. I," *Phys. Rev.* **85**(2), 166–179 (1952).
47. K. F. M. G. Galloway and T. J. Russell, "A simple model for separating interface and oxide charge effects in MOS device characteristics," *IEEE Trans. Nucl. Sci.* **36**(6), 1497–1501 (1984).
48. P. J. McWhorter, P. S. Winokur, "Simple technique for separating the effects of interface traps and trapped-oxide charge in metal-oxide-semiconductor transistors," *Appl. Phys. Lett.* **48**(2), 133–135 (1986).
49. R. Castagne and A. Vapaille, "Description of the SiO₂/Si interface properties by means of very low frequency MOS capacitance measurements," *Surf. Sci.* **28**(1), 157–193 (1971).

1. Introduction

In recent years, transparent conductive oxides (TCOs) have attracted escalating research interests as a new type of plasmonic materials [1–2]. TCOs, such as indium-tin oxide (ITO) and aluminum-zinc oxide (AZO), are a family of wide bandgap semiconductor oxide materials that can be degenerately doped to a high level, which are widely used in display industry [3] and photovoltaics [5]. Compared with typical semiconductor materials such as silicon and III-V compound semiconductors, TCOs possess several unique optical properties as plasmonic materials in the telecom wavelength range. First, the free carrier concentrations can reach as high as $1 \times 10^{21} \text{ cm}^{-3}$ by degenerate doping or by a gate voltage. Therefore, the real part of the refractive index could experience more than unit refractive index unit (RIU) change [5]. Second, the high frequency permittivity of TCOs (~ -4) is usually much lower than that of Si or III-V semiconductors (>12). With free carrier concentration above $6.5 \times 10^{20} \text{ cm}^{-3}$, the real permittivity of TCOs reaches zero while the absolute permittivity is a minimum value due to the small value of the imaginary part. Such unique optical properties, called epsilon-near-zero (ENZ), will dramatically enhance the light-matter interaction and have been intensively investigated with TCO materials [6–9]. When ENZ materials are integrated with regular dielectric or metallic materials, the electric field polarized perpendicular to the interface will be strongly confined in the ENZ layer due to the continuity of electric field displacement and ultra-high light absorption is expected [10–12]. Although in theory, it is also possible to turn Si or III-V semiconductors into ENZ with extremely high free carrier concentration ($>2 \times 10^{21}$) based on Drude model, the required electric field will far exceed the breakdown strength of any known insulator material. In practice, it is still far from ENZ for Si even at 10^{21} cm^{-3} free carrier concentration due to the large value of its high frequency permittivity. Third, the electron mobility of TCOs ($40\text{--}300 \text{ cm}^2/(\text{V}\cdot\text{s})$) is much lower than that of single crystal Si ($\sim 1400 \text{ cm}^2/(\text{V}\cdot\text{s})$), which translates into a much larger damping factor. As the free carriers accumulate, the imaginary part κ of TCOs increases to the same order of magnitude as the real part, which causes dramatic increase of the optical absorption that is $30\text{--}140 \times$ larger than that of silicon [13]. Such high optical absorption is detrimental to passive optical waveguides, but will benefit electro-absorption (EA) modulators to be discussed in this paper. As comparison, single crystalline semiconductors such as Si and GaAs can only effectively absorb light at the ENZ condition, which is very difficult to achieve due to the high optical permittivity. Moreover, such high carrier mobility will also result in narrower optical bandwidth and the modulation depth deviating from the ENZ wavelength can be much lower than that at the ENZ wavelength. Therefore, free carrier absorption is not a good mechanism for Si or GaAs modulators.

Realizing the great potential to build wavelength-scale EA modulators, various groups have designed TCO based gate-driven ENZ modulators [14–26], which are exclusively built upon the concept of integrating metal-oxide-semiconductor (MOS) capacitor with silicon or plasmonic waveguides. These modulators follow the same working principal: the gate voltage

induces electron accumulation in the TCO materials, which dramatically increases the imaginary part κ or even turns TCOs into ENZ to achieve strong light absorption. Although many optical waveguide structures have been proposed, such as metal-insulator-metal (MIM) waveguides and silicon ridge and slot waveguides, there are only three basic MOS capacitor structures among all these designs as shown in Fig. 1: a) metal/insulator/TCO, b) metal/TCO/insulator/Si or metal/insulator/TCO/Si, and c) TCO/insulator/Si. Depending on the waveguide design, TCO materials and the modeling of the MOS capacitor, especially the assumption of the thickness of the accumulation layer (ACL) and the distribution of the free carriers in the TCO materials, the EA rate, which is defined as the extinction ratio over the electrode length, varies from 0.1~18 dB/ μm in the reported simulation results. In parallel to the design and simulation, some experimental work of TCO modulators has also been published in the last a few years [13, 27–31]. Different than simulation results based on free carrier concentrations, experimental results have to be measured by the driving voltage. Therefore, the modulation strength, which is defined as the extinction ratio divided by the product of the electrode length and the driving voltage with the unit of dB/($\mu\text{m}\cdot\text{V}$), will measure the TCO EA modulator more accurately. However, the modulation strength strongly depends on the waveguide dimension and the configuration of the MOS capacitors. The modulation strength is reported to be 0.2~1.2 dB/($\mu\text{m}\cdot\text{V}$) in existing papers [27–31], which shows far less variation than simulation.

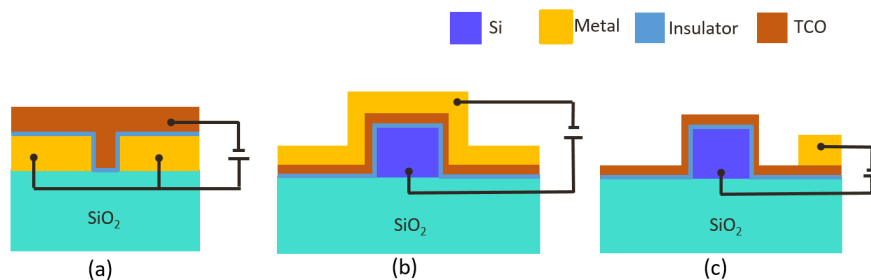


Fig. 1. Illustration of the MOS capacitor designs for TCO EA modulators: (a) Au/insulator/TCO, (b) Au/TCO/insulator/Si, and (c) TCO/insulator/Si. Waveguide design may vary in different references.

This manuscript is organized in the following way. In Section 2, we discuss and compare several representative modeling papers using uniform concentration accumulation layer (termed as “uniform concentration model”) and classical continuous carrier distribution from traditional semiconductor physics (termed as “classical model”). We also analyze the variation of the EA rate and calculate the driving voltage, electric field in the insulator and the modulation strength using the simple parallel-plate capacitor approximation for the uniform concentration accumulation carrier model. The correlation of the waveguide type, ACL thickness, insulating layer dielectric constant and thickness to the EA rate and modulation strength are discussed with extension to the trade-off with driving voltage and device reliability. In Section 3, we apply the quantum moment model to simulate the free carrier accumulation of an ITO/HfO₂/p-Si MOS capacitor. At 1.55 μm wavelength, the quantum moment model simulation suggests significant deviation in terms of the ACL thickness and the required driving voltage from the classical model, which may lead to different perspectives toward TCO based ENZ devices. The quantum model is also applied to the Au/HfO₂/ITO waveguide and the simulated carrier distribution is integrated with 2-D finite element method (FEM) optical mode solver to show the optical mode profile at ENZ condition along with the comparison to that of uniform concentration model with 1 nm uniform thickness and classical model. In Section 4, we review the experimental results of TCO EA modulators in recent years and compare two most recent experimental papers working at telecom wavelength of 1.55 μm to the simulation results using different models.

The comparison shows that the quantum model matches the experimental results better than the classical model, but still cannot fully explain the results from some other papers. We attribute the discrepancy to other modulation mechanism, which is not conclusive and we are open to further discussion. Section 5 summarizes the conclusion and contribution of this paper briefly.

2. Existing simulation models

There are two existing approaches to model the free carrier accumulation in TCO based MOS capacitors. The first model, uniform concentration model, assumes uniform concentration of the ACL with hypothesized thickness ranging from 1 to 10 nm based on different theories [14–23] while the MOS capacitor is simplified into a parallel dielectric plate capacitor with thickness equal to the insulator thickness. For example, 1 nm ACL thickness was accepted in Ref [14–16] based on the approximation of the Thomas-Fermi screening effect [32]. Thicker accumulation layer using different theories of approximation can lead to much higher absorption rate as the ENZ region has a larger overlap with the waveguide mode. However, it also requires much higher driving voltage as the total amount of accumulated charge will increase proportionally, which can lead to the breakdown of the insulator layer. The first part of Table 1 summarizes the representative, although not an exhaustive list of the TCO EA modulator designs using uniform concentration model in recent five years, in which the columns of waveguide type, waveguide width, ACL thickness, ENZ free carrier concentration N_{ENZ} , EA rate, oxide material and thickness are parameters directly obtained from those papers. For the uniform concentration model, there are two general trends. First, the EA rate increases as the ACL thickness increases since the ENZ layer will have a larger optical mode overlap with the waveguide. Second, hybrid plasmonic-silicon or metal-insulator-metal (MIM) waveguides can significantly improve the EA rate due to the ultra-high optical mode confinement from plasmonics [33]. Most uniform ACL simulation papers focus on the electro-absorption at ENZ under the assumption of different thickness of the accumulation layer. However, the driving voltages to reach the ENZ condition were not adequately addressed. In this paper, we use a simple parallel-plate capacitor model to calculate the driving voltage. The unit area capacitance of the MOS capacitor in the accumulation mode is approximated as:

$$C = \frac{\epsilon_0 \epsilon_r}{d_{ox}} \quad (1)$$

where ϵ_0 is the permittivity of vacuum, ϵ_r is the dielectric constant of the insulator, and d_{ox} is the thickness of the insulator. The driving voltage required to reach ENZ is defined as:

$$V = \frac{Q_{ENZ}}{C} = \frac{N_{ENZ} d_{ACL}}{C} \quad (2)$$

where N_{ENZ} is the free carrier concentration for the TCO to reach ENZ and d_{ACL} is the thickness of the accumulation layer. The values of N_{ENZ} and d_{ACL} are listed in Table 1. The electric field across the insulator at the ENZ condition, which is the column of the estimated electric field in the insulator in Table 1, is estimated as:

$$E = \frac{V}{d_{ox}} \quad (3)$$

As shown in Table 1, it is very clear that as the presumed ACL thickness increases, many of the simulated electric fields across the insulator exceed the breakdown strength of common insulator materials such as SiO_2 (10 MV/cm), Al_2O_3 (7 MV/cm), and HfO_2 (5 MV/cm) [34]. The second approach, classical model, calculates the carrier distribution as a stationary solution using a classical semiconductor device model by considering the quantum pressure at

the semiconductor-insulator interface. From the simulation results, the maximum carrier density occurs at the ITO/HfO₂ interface and decays exponentially with a steep slope. Also the MOS modeling results show that the peak carrier concentration can reach the requirement of ENZ ($\sim 6.5 \times 10^{20} / \text{cm}^3$) with reasonable driving voltage when using a thin high dielectric constant insulator material such as HfO₂.

Table 1. Comparison of modeling results of TCO EA modulators

Uniform concentration model									
Ref	Waveguide type	Waveguide width (nm)	ACL thickness (nm)	N_{ENZ} (cm^{-3})	EA rate ($\text{dB}/\mu\text{m}$)	Oxide material and thickness	Estimated electric field in insulator (MV/cm)	Estimated applied voltage (V)	Modulation strength ($\text{dB}/\mu\text{m}/\text{V}$)
[14]	Hybrid Au-Si slab waveguide	$H_{\text{si}} = 290$	1	$\sim 1.0 \times 10^{21}$	4	HfO ₂ , 5 nm	7.2	3.6	1.1
[15]	Si ridge waveguide	$H_{\text{si}} = 400$	1	6.3×10^{20}	0.11	HfO ₂ , 5 nm	4.6	2.3	0.048
[16]	Si slot waveguide	$W_{\text{slot}} = 20$	1	$\sim 1.0 \times 10^{21}$	4.5	HfO ₂ , 5 nm	13	6.5	0.69
[17]	MIM waveguide	$W_{\text{slot}} = 8$	3	6.5×10^{20}	15.2	HfO ₂ , 5 nm	8	4	2.5
[18]	Si slab waveguide	$H_{\text{si}} = 220$	3	8.0×10^{20}	4.3	HfO ₂ , 5 nm	2.6	1.3	3.3
[19]	Si slot waveguide	$W_{\text{slot}} = 30$	5	6.7×10^{20}	8.9	Si ₃ N ₄ , 7 nm	28.2	19.7	0.45
[20]	Si slot waveguide	$W_{\text{slot}} = 20$	5	7.1×10^{20}	17.4	SiO ₂ , 10 nm	67.0	67.0	0.26
[21]	Si slot waveguide	$W_{\text{slot}} = 20$	5	9.4×10^{20}	6.6	Si ₃ N ₄ , 10 nm	147	147	0.045
[22]	IMI waveguide	$W_{\text{slot}} = 30$	7	6.8×10^{20}	6	SiO ₂ , 20 nm	217	434	0.014
[23]	Hybrid Au-Si ridge waveguide	$H_{\text{si}} = 200$	10	6.8×10^{20}	8	SiO ₂ , 20 nm	310	620	0.013
Classic semiconductor model									
		Waveguide width (nm)		N_{ENZ} (cm^{-3})	EA rate ($\text{dB}/\mu\text{m}$)	Oxide material and thickness	Estimated electric field across oxide (MV/cm)	ENZ voltage	Modulation strength ($\text{dB}/\mu\text{m}/\text{V}$)
[24]	Hybrid Au-Si ridge waveguide	$H_{\text{si}} = 400$		6.5×10^{20}	1.7	HfO ₂ , 10 nm	1.5	1.5	1.1
[25]	MIM waveguide	$W_{\text{slot}} = 5$		$\sim 1 \times 10^{21}$	20	HfO ₂ , 2.5 nm	40.4	2.6	7.7
[26]	Si slot waveguide	$W_{\text{slot}} = 10$		6.2×10^{20}	1.9	HfO ₂ , 5 nm	6	3	0.63
	Si slab waveguide	$W_{\text{si}} = 180$			0.5				0.16

The summary in Table 1 shows the EA rate as well as the modulation strength of the TCO EA modulator, which is defined as the EA rate divided by the driving voltage with unit of $\text{dB}/(\mu\text{m} \cdot \text{V})$. For the same type of waveguide structure, the EA rate calculated by the classical

model is generally lower than that obtained by uniform concentration model, even at 1 nm thickness. This is understandable since the classical model gives a very steep profile slope of the free carrier distribution and the effective ENZ layer is much thinner. More significantly, as shown by U. Koch et al. in Fig. 8 of Ref [24], the classical model predicts a digital transfer function with two well-defined states. In other words, the maximum EA will saturate as the driving voltage reaches above that for ENZ. As a comparison, uniform concentration model presents strongly enhanced EA rate at the ENZ voltage like a resonator, which is caused by the field enhancement in an unphysically thick layer. Such unexpectedly high EA and the resonator-like features at relatively low driving voltage have never been experimentally observed.

3. Quantum moment model

We apply the quantum moment model [35] to simulate the free electron accumulation of TCO MOS capacitors and the simulated carrier distribution is integrated with 2-D finite element method (FEM) optical mode solver to calculate the modulation strength of two existing designs. Quantum moment model, also named as density gradient model, is based on the moments of the Wigner function equation of-motion [41-42], which consists of quantum correction to the carrier temperatures in the carrier current and energy flux equations. Quantum moment model can solve the problems of thin gate oxide MOS capacitors and transistors more accurately than semi-classical device model. In order to turn the TCO material into ENZ, a thin high dielectric constant gate insulator layer is preferred. As a high electric field is applied across the oxide, a narrow and deep triangular potential well as shown in Fig. 2 (a) is induced at the interface [36]. The key feature is that near the interface, a fast varying contribution from the band-edge-offset and a comparatively slow varying contribution from the electric potential can be separated. If the energy step at the band edge is large enough, it can be considered as an infinite barrier. For the conduction band, the band off-set at the ITO/HfO₂ interface (~5 eV) is large compared to a typical carrier energy in ITO, which is usually a few k_bT , where k_b is the Boltzmann constant and T is the temperature. Therefore, it is appropriate to assume an infinite potential barrier at the ITO/HfO₂ interface and a triangular potential well. According to the quantum-mechanics theory, in such a potential well, the kinetic energy of the carriers in the direction perpendicular to the surface is quantized and the problem can be solved by density gradient model [35]. In the density gradient model, the expression for electron current is given by:

$$\mathbf{J}_n = qD_n \nabla n - qn\mu_n \nabla(\Psi - \Lambda) - \mu_n n \{kT_L \nabla[\ln(n_{ie})]\} \quad (4)$$

Here n_{ie} is the intrinsic concentration, T_L is the lattice temperature, and Λ is a quantum correction potential [46]. The final term accounts for the gradient in the effective intrinsic carrier concentration, which takes account of bandgap narrowing effects. The quantum potential can be calculated using the expression given in

$$\Lambda = -\frac{\gamma \hbar^2}{6m} \frac{\nabla^2 \sqrt{n}}{\sqrt{n}} \quad (5)$$

where γ is a fit factor, m is the carrier effective mass, and n represents electron or hole concentration as appropriate.

To solve the carrier distribution using quantum model, we implemented a 1-D ITO/HfO₂/p-Si structure in Silvaco [37]. The quantum model in Silvaco can be applied to both accumulation and depletion mode to solve the electron charge distribution of MOS capacitors at nanometer scale. The material parameters of ITO and Si are summarized in Table 2:

Table 2. Material parameters for the Si and ITO semiconductors

Parameter	Band gap (eV)	Electron mobility (cm ² /(V·s))	Electron affinity (eV)	Relative static permittivity	N _c (/cm ³)	N _v (/cm ³)
ITO	3.8 [38]	35	5 [39]	9 [40]	5 × 10 ¹⁸	...
Si [37]	1.08	1000	4.17	11.8	2.8 × 10 ¹⁹	1.04 × 10 ¹⁹

In Table 2, N_c and N_v denote the effective density of states of the conduction band and valance band. The mobility of ITO was measured by Hall measurement. N_v for ITO is not reported since it is a degenerately n-doped semiconductor and does not play any meaningful role in our simulation. N_c of ITO is calculated by the following equations:

$$N_c = 2 \left[\frac{2\pi m_e^* kT}{h^2} \right]^{3/2} \quad (6)$$

where m_e^* is the effective mass of electron and equals to 0.35 m_0 . The bulk carrier concentration of ITO and Si is 1×10^{20} /cm³ and 1×10^{17} /cm³, respectively. The thickness of HfO₂ is 10 nm. Next, the built-in density gradient model in Silvaco for holes and electrons were activated to compute the carrier distribution at different bias.

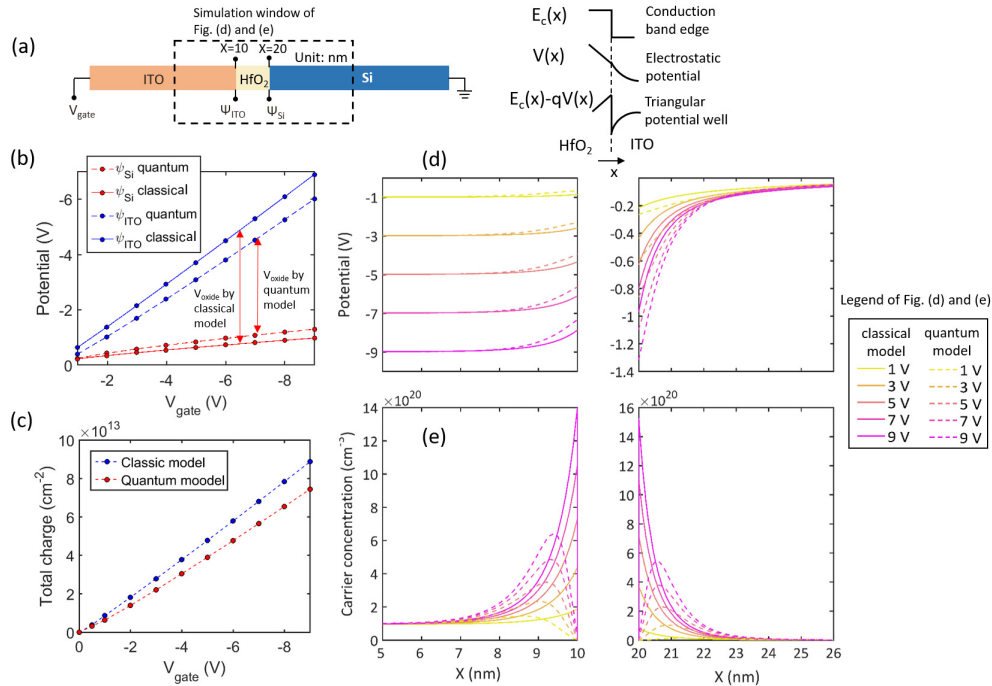


Fig. 2. (a) Schematic and electric potential of the ITO/HfO₂/p-Si MOS capacitor; (b) electric potential at the Si/HfO₂ interface and the ITO/HfO₂ interface using classical and quantum model; (c) total accumulated charge of the MOS capacitor calculated by classical and quantum model; (d) electric potential distribution and (e) carrier concentration distribution under different gate voltages using classical (solid line) and quantum model (dashed line).

Figure 2(a) shows the schematic of the TCO/HfO₂/p-Si MOS capacitor, in which the TCO is based on the definition of indium-tin-oxide (ITO). In this configuration, Si is grounded, ψ_{Si} represents the electric potential at the Si/HfO₂ interface and ψ_{ITO} represents the electric

potential at the ITO/HfO₂ interface. The double-arrow lines mark the voltage drop across the insulator layer. Both quantum moment model and classical model shows that the voltage drop in ITO and Si is not negligible, which means only part of the applied voltage drops across the insulator. Therefore, uniform concentration model in Table 1 overestimated the electric field in the insulator and actual devices may withstand higher driving voltage than simple parallel-plate capacitor model. Figure 2(b) also shows that the voltage-drop in the insulator predicted by the quantum model is smaller than that by the classical model. Figure 2(c) shows the total amount of accumulated charge as a function of the applied gate voltage. It is very interesting to point out that the total amount of charge calculated by the quantum model is about 15% less than that by the classical model, which is attributed to the smaller electric field across the insulator. Figure 2(d) and (e) shows the electric potential distribution and free carrier distribution in ITO and silicon using the classical and quantum model.

First, the most important effect of the quantization of the kinetic energy of carriers at the interface is a significant change in the electronic charge distribution in ITO and silicon. Namely, the classical model and quantum model use different approaches to satisfy the boundary condition of $j_z(x, z = 0) = 0$ at the interface, which was explicitly explained in ref [36] by W. Hansch et.al. The classical approach achieves this by placing the carrier density maximum at the interface. Therefore, the drift and diffusion current cancel out. For the quantum model, the normal component of the current will not vanish at the interface if the classical drift diffusion approximation is utilized, because drift and diffusion current have the same sign. Instead, the quasi-Fermi level will not approach the surface with zero slope and the classical current must be corrected to guarantee a vanishing current perpendicular to the interface. This requirement results in the pin-down of the carrier concentration at the interface and several angstroms of shift of the peak concentration into the semiconductor layer. The shift of the charge maximum effectively increases the thickness of the insulating layer as the centroid of the charges in ITO and silicon are separated further away from each, which decrease the capacitance of the MOS capacitor. Second, the charge distribution of the quantum model is much wider than that predicted by the classical model. The greater width of the charge distribution has also the effect of substantially modifying the semiconductor voltage distribution. In particular, the voltage drops in ITO and silicon predicted by the quantum model is much larger than that by the classical model.

As a consequence of those differences, we will derive significant differences for TCO EA modulators by the quantum and classical models. First, it requires much higher driving voltage to turn TCO into ENZ due to the wider spread of the accumulated free carriers (major reason) and the reduced capacitance (minor reason). Second, as the quantum-model-simulated charge distribution is much wider and resembles a peak shape rather than a monotonously decreasing distribution, the equivalent ENZ layer thickness will be much larger than the classical model verified in Fig. 3(c) and (d). Therefore, the EA rate at ENZ obtained by the quantum model should be larger than that by the classical model. Both of these conclusions are verified in Section 4.

Following the quantum modeling, we evaluated the effect of carrier distribution to the optical waveguide in terms of optical field distribution. In the “ON” state, which is defined as when the gate voltage is 0 V, the waveguide mode is simulated by Lumerical MODE to obtain the propagation loss as the reference. In Fig. 3, we use MIM waveguide with Au/HfO₂/ITO MOS structure as an example to show the difference of the mode profile calculated by different models. The “ON” state 2-D waveguide mode profile is shown in Fig. 3(a). Subsequently, the distribution of the optical permittivity was calculated using Drude model by obtaining the spatial free carrier distributions at different gate voltages. The spatial optical permittivity results obtained by the quantum and classical model of ACL were then imported into Lumerical MODE solver to perform the optical simulation and calculate the corresponding effective index of the waveguide mode. For uniform concentration model, we first computed the total charge at different gate voltage based on quantum model and then

averaged it such that we had a uniform carrier concentration with ACL of 1 nm thickness. All carriers accumulated in the ACL while the rest of the ITO remained unaffected. Then the Drude model was used to translate the carrier concentration changes into the refractive index distribution. Optical simulation then was performed to obtain the propagation loss and electric field distribution. In Fig. 3(b), 2-D waveguide modes for the “OFF” state are plotted to illustrate the electro-absorption. We can further understand the difference between the three models by looking at the waveguide cross-sectional mode profiles in the “OFF” state. Since the accumulation layer is very thin and the waveguide is majorly transverse electric (TE) mode, the zoomed-in view of the optical permittivity profile and the optical field intensity along the horizon direction of the mid-height Au/HfO₂/ITO (along a-a”) are shown in Fig. 3(c)-(d) for 1nm uniform concentration model, quantum model and classical model. For all three models, the optical mode profiles show peak intensity at the ITO/HfO₂ interface because of the well-known ENZ effect. The difference between these three models is the ENZ layer thickness due to different assumptions of the free carrier accumulation.

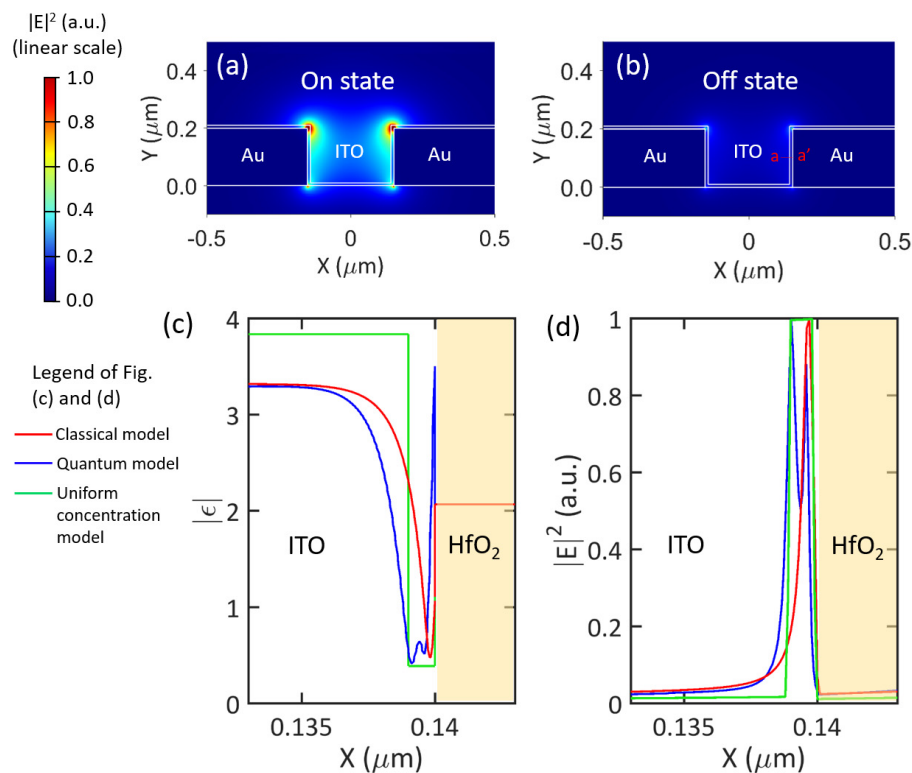


Fig. 3. 2-D Electric field distribution of the 2-D waveguides at (a) “ON” and (b) “OFF” state with 1-D zoomed-in view; zoomed-in view of the absolute value (c) and optical field intensity (d) of the MIM waveguide at “OFF” state obtained by 1nm uniform concentration model (green line), quantum model (blue line), and classical model (red line).

4. Comparative analysis

In order to evaluate the accuracy of each model, we did a comparative analysis with some experimental results of TCO EA modulators. Table 3 summarizes the most representative experimental work in terms of EA rate and modulation strength. It is interesting to point out that all these experimental results involve plasmonic waveguide structures to enhance the light-matter interaction. For the sake of optical losses, however, most plasmonic waveguides use relatively large feature size around 300 nm. The EA rates of these reported TCO EA modulators range from 1.0~2.9 dB/ μm , which are roughly on-par with 1 nm uniform

thickness model, classical model and quantum model. However, uniform thickness model with 3nm and above significantly overestimated the EA rate (>4 dB/ μm) due to the unrealistic assumption of the accumulation layer thickness.

Table 3. Summary of experimental results of TCO EA modulators

Ref.	Waveguide type	Waveguide width (nm)	Voltage (V)	EA rate (dB/ μm)	Oxide material and thickness	$\epsilon_{r,ox}/d$ (/nm)	Modulation strength (dB/ $\mu\text{m}/\text{V}$)	Normalized modulation strength (dB·nm/ $\mu\text{m}/\text{V}$)
[27]	MIM waveguide	$W_{\text{slot}} = 300$	2.2	2.7	Al_2O_3 , 5nm	2.3	1.2	0.52
[28]	Hybrid Au-Si ridge waveguide	$H_{\text{Si}}=340$, $W_{\text{Si}} = 800$	4.0	1.0	SiO_2 , 20 nm	0.2	0.25	1.3
[29]	Hybrid Au-Si slab waveguide	$H_{\text{Si}}=290$, $W_{\text{Si}} = 400$	6.0	2.5	HfO_2 , 5 nm	5	0.42	0.084
[30]	MIM waveguide	$W_{\text{slot}}=50$	14.0	2.88	HfO_2 , 20 nm	1.25	0.21	0.17
[31]	MIM waveguide	$W_{\text{slot}} = 300$	3.5	1.5	HfO_2 , 10 nm	2.5	0.43	0.17

To further study these models quantitatively, we simulate the absorption rate as a function of the gate voltage for the waveguide and MOS structure in Ref [29] and [31] using 1 nm uniform concentration model, the classical model and quantum model, respectively. The simulation results in comparison with experimental data are plotted in Fig. 4(a) and (b) corresponding to the waveguide structure of Fig. 1(b) and (a), respectively, for both the depletion mode and accumulation mode. One of the main difficulty to plot the experimental results in Fig. 4(a) and (b) is how to select the initial gate voltage. If the device starts from the flat-band state with no accumulated charges at the interface, we should not see a measurable extinction ratio in the -3 to $+2$ V voltage range of the $-V_{\text{gate}}$. It means that the absorption rate in the depletion or weak accumulation is very small. However, most experimental results show a quite linear increase of the absorption rate vs. V_{gate} . Therefore, we believe that there are accumulated charges even when the applied bias voltage is zero. In other words, the devices start from the accumulation mode already, which is very likely due to the surface charges as discussed in Ref [47–49], since the TCO/ HfO_2 interface may induce trapping states or other type of defects. It is true that the DC offsets of these devices are quite large and the interface between TCO/ HfO_2 definitely requires more in-depth research. In addition, the actual doping concentration of the TCO may not be exactly the same as designed, which can also affect the gate voltage. Therefore, we used an empirical method to determine the initial gate voltage by matching the slope of the curve, which is the differential between the EA rate over the gate voltage, to that of the 1 nm uniform concentration model. We acknowledge that this empirical method will induce some error in the DC offset, however, it is still helpful to evaluate the trend of each model based on the differential voltage. From Fig. 4(a) and (b), it is very obvious that the resonator-like enhanced EA rate predicted by the 1 nm uniform model at relatively low voltage does not match experimental results. For classical model, the digital modulation by a small gate voltage is not observed either. In addition, the classical model predicts a saturated EA rate at about 1.2 dB/ μm , which is far less than the experimental results. In comparison, quantum model results have the best match with experimental data in terms of the overall trend and maximum EA rate. For the quantum model, it predicts a gradual decrease of the EA rate above ENZ that is not observed in experiment. This is most likely caused by the breakdown of the insulator layer, which prohibits experimental implementation at such high gate voltages. In addition, thermal effects and carrier trapping may induce additional loss at such high electric field, which can prevent the decrease of the absorption rate.

Last, we would like to point out that the dielectric constant and thickness of the insulator plays the most critical role to affect the modulation strength since it determines the unit area capacitance of the device. A higher dielectric constant and thinner layer insulator will induce more charge given the same gate voltage and hence achieving higher modulation strength. Since the modulation strength can be significantly improved by high dielectric constant insulator and thinner insulator thickness, we define the “normalized modulation strength” in Eq. (6), which will exclude such effects and can compare the device performance that is only determined by the waveguide structure. Thus the normalized modulation strength should have a better representation of the TCO EA modulators.

$$\text{Normalized modulation strength} = \frac{\text{modulation strength}}{\epsilon_{r,ox} / d} = \frac{EA \text{ rate} / V}{\epsilon_{r,ox} / d} \quad (6)$$

The normalized modulation strength is relatively constant in [29–31], which is 0.08–0.17 dB·nm/μm/v with acceptable variation due to the difference in waveguide geometries. However, Ref [27–28] shows abnormally large normalized modulation strength of 0.52–1.25 dB·nm/μm/v, which cannot be explained by the difference of waveguide designs. Actually, the experimental results in Ref [27–28] cannot be quantitatively matched to any existing model as discussed in this paper. We speculate that the abnormally large modulation strength may partly come from different E-O modulation mechanisms, such as the conductive path formation through the insulator layer due to metal ion transport [43–44], rather than the EA absorption from the free carrier accumulation. However, this argument is not conclusive and further discussion is beyond the scope of this paper.

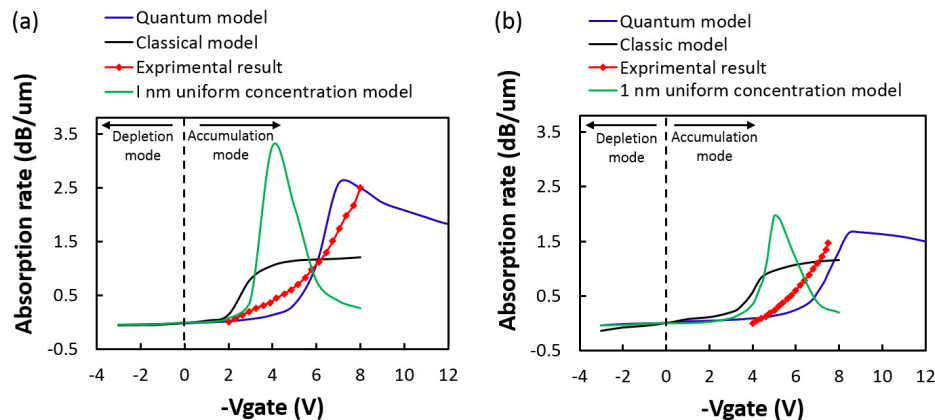


Fig. 4. Simulation and experimental results of the modulation strength as a function of the gate voltage for (a) hybrid plasmonic-silicon ridge waveguide [29] and (b) MIM waveguide [31].

5. Summary

In summary, we conducted a comparative analysis of TCO-EA modulators using uniform concentration free carrier model, classical semiconductor device model, and quantum moment model. Indeed, our modeling shows that the EA modulation strength obtained from the quantum moment model matches the experimental results better than other modeling methods in terms of the overall trend and maximum EA rate. More importantly, our quantum moment model simulation results reveal new device physics that can be pertinent to the whole research community working on TCO based ENZ devices. The quantum moment model predicts a much higher driving voltage in order to turn the TCO materials into epsilon-near-zero and a stronger modulation strength compared with the classical model. Especially, the requirement of higher gate voltage brings a great challenge to the insulator layer as the electric field in the

insulator is very close or even exceeding the breakdown strength, which raises the concern of device reliability. Further investigation of E-O modulation mechanisms in TCO devices is necessary, which may explain some abnormally large “ENZ” effects.

Funding

AFOSR MURI Project (FA9550-17-1-0071).